A multigrid PGD-based algorithm for volumetric displacement fields measurements

Luis Agnaldo Gomes Perini, Jean-Charles Passieux, Jean-Noël Périé

A multigrid PGD-based algorithm for volumetric displacement fields measurements

L.A. Gomes Perini, J.-C. Passieux, J.-N. Périé

Université de Toulouse ; Institut Clément Ader ; INSA, UPS, Mines Albi, ISAE;
3 rue Caroline Aigle F-31400 Toulouse, France

ABSTRACT: The use of a finite elements based Digital Volume Correlation (FE-DVC) leads to lower measurement uncertainties in comparison to subset-based approaches. However, the associated computing time may become prohibitive when dealing with high resolution measurements. To overcome this limitation, a PGD solver was recently applied to 2D digital image correlation. In this paper, this method is extended to measure volumetric displacements from 3D digital images. In addition, a multigrid PGD algorithm is developed, which allows to use different discretizations in each term of the decomposition. Associated to a coarse graining of the digital images, this allows to avoid local minima, especially in presence of large displacements. Synthetic and practical cases are analyzed with the present approach and measurement uncertainties are compared with standard FE-DVC. Results show that such an approach reduces the computational cost (when compared to FE-DVC) while maintaining lower measurement uncertainties than standard subset-based DVC.

KEY WORDS: Digital image correlation, Digital volume correlation, Full-field kinematic measurements, Multigrid, Proper Generalized Decomposition

Introduction

Today, heterogeneous materials are intensively studied in many engineering fields (as aeronautics, automobile, marine and biomechanics). Their effective properties calls for 3D micro/macro-mechanical characterization [11]. Consequently, volumetric full-field measurements may be convenient, since a large amount of information can be retrieved through a reduced number of experiments (when compared with classical instrumentation techniques).

Among the full-field displacement measurement methods, the Digital Volume Correlation (DVC) [3] (which is a 3D extension of the Digital Image Correlation - DIC - technique [36]) has been applied to many materials over the last years, such as trabecular bone [3, 4], wood [11], granular materials [21, 34], cast iron [20, 30], and stone wool [13], for instance. Since it is a non-contact technique, DVC is very attractive in experimental conditions where classical instrumentation techniques may be unsuccessful. Basically, it compares a sequence of textured 3D images of the same object (under different loading conditions) in order to obtain the associated displacement field of a chosen region of interest (ROI). Any volumetric images acquired by any imaging techniques, like Magnetic Resonance Imaging (MRI) or computed tomography (CT), can be used.

Recently, a global formulation of DIC/DVC was proposed by [5, 31], which seeks the displacement field over an entire ROI. It relies on a weak formulation of the assumption of brightness conservation [16], leading to the inversion of a system whose solution yields the displacements over the entire ROI. The interpolation of this displacement field can be varied. An interesting route

consists in using Finite Elements (FE) shape functions (FE-based DIC/DVC) [5, 35, 31, 9]. It thus enables a direct link with numerical simulations. It can be helpful during the identification and validation of constitutive laws and numerical models [15]. However, the high number of degrees of freedom (DOF) associated to refined meshes or large structures, can lead to computing time issues [20, 27]. As an example, a 3D image of $1000 \times 1000 \times 1000$ voxels may lead to more than 10^6 DOF when using elements size of 10 voxels. This requires the inversion of a large system at each iteration in classical FE-based algorithm, whose computational cost may become significant.

These issues have already been addressed in computational mechanics. For instance, the Proper Generalized Decomposition method (PGD) [1, 18] has been employed to speed-up the resolution of complex problems, enabling to obtain solution to problems that could not be addressed before. It uses a separated representation of a multi-dimensional function. Specifically, it consists in approximating an N-dimensional function as a sum of products of k-dimensional functions, with $k < N$. This method was originally used for treating space-time problems [17]. It has been extended to multi-dimensional problems like complex fluids modeling [1], stochastic simulations [23], multi-scale problems [25], parametric models [29], structural dynamics [7], 3D-spatial models [6] and numerical homogenization [12], for instance. For a comprehensive review of PGD applications, readers may refer to [8].

In [27], PGD is integrated with DIC in order to speed-up measurements of 2D displacements fields. The unknown displacement field, sought as a sum of products of uni-dimensional functions, is corrected at each approximation of the correlation problem using a fixed-point algorithm. This new method, denoted PGD-DIC, requires only 1D meshes in each dimension, reducing the numerical complexity. It preserves all the advantages of the FE-DIC approaches (such as the continuity and the direct link with numerical simulations) at the same time it reduces their main drawback, namely the associated computational cost.

In this paper, we propose to extend this technique to measure 3D continuous volumetric displacement fields, to cope with the expected computational issue. It is based on the 2D formulation proposed by [27]. The unknown displacement field is sought as a sum of products of uni-dimensional functions in the three spatial dimensions. When inserted in the DVC formulation, a coupled system (one problem for each spatial dimension) is obtained. A fixed point algorithm (or alternating dimension algorithm) is used to solve these problems independently. Only few iterations of this algorithm are enough to compute a new best rank one approximation, which is used to compute the linear prediction of the correlation problem. Hence, the computational time associated to the inversion of the FE system is further reduced.

More than that, a multigrid PGD algorithm is devised in this paper. It allows to use different discretizations in each term of the sum in the PGD approximation. Therefore, one can use coarser meshes at the early iterations and refine them during convergence. This algorithm is associated to a coarse graining of the volumetric digital images. As studied in [5, 9, 33, 14], it improves convergence and also avoids local minima, which occurs for instance when large displacement magnitudes are involved.

This article is organized as follows. Section 2 recalls the main features of the global DVC formulation. Section 3 presents the basis of PGD and how it is integrated with DVC. The multigrid strategy and a regularization method are also presented. Section 4 validates the proposed method by comparing the uncertainties associated with the FE-based DVC (considered as reference) and analyses a synthetic example. In Section 5 the method is used to measure volumetric displacement measurements in a trabecular bone subjected to compression [4]. The results are compared to those obtained from a FE-based DVC. Finally, in Section 6, the characteristics of the proposed method are discussed and new perspectives are exposed.

Digital Volume Correlation (DVC)

Digital Volume Correlation was firstly introduced in [3]. It basically consists in a volumetric extension of subset based approaches classically used for DIC. In this section, the main principles of a more recent global formalism [5, 31] are presented.

The main idea behind DVC is to determine the optical flow between image sequences, assuming the brightness conservation [16]. Let us consider two different volu-

metric images of the same object $f(\mathbf{x})$ (at rest) and $g(\mathbf{x})$ (after loading), where $\mathbf{x}$ is the position of a point in the image. Each image f and g collects the gray level of each position $\mathbf{x}$, and, under the hypothesis of gray level conservation, they are related by:

$$f(\mathbf{x}) = g\left(\mathbf{x} + \mathbf{u}(\mathbf{x})\right) \tag{1}$$

where $\mathbf{u}(\mathbf{x})$ denotes the unknown displacement field. This three-components vector reads:

$$\mathbf{u}(\mathbf{x}) = \mathbf{u}(x,y,z) = \begin{pmatrix} u(x,y,z) \\ v(x,y,z) \\ w(x,y,z) \end{pmatrix} \tag{2}$$

Determining the displacement field that verifies the assumption (1) is an ill-posed problem. In practice, the gray level information of images f and g is indeed not sufficient to determine all the displacement components at each voxel. Then, a classical sum of squared differences computed over the entire ROI (Ω) is prefered:

$$\Phi^2 = \int_\Omega \left[f(\mathbf{x}) - g(\mathbf{x} + \mathbf{u}(\mathbf{x}))\right]^2 \, d\mathbf{x} \tag{3}$$

The problem turns out to find the best $\mathbf{u}(\mathbf{x})$ that minimizes (3). Because of the nonlinearity of this equation, an iterative process is employed assuming that the correction of the displacement field, $\delta\mathbf{u}(\mathbf{x})$, at each iteration m, is small enough to allow for a first order Taylor expansion:

$$g(\mathbf{x}+\mathbf{u}_m(\mathbf{x})) \approx g(\mathbf{x}+\mathbf{u}_{m-1}(\mathbf{x}))+\delta\mathbf{u}(\mathbf{x})^T\nabla g(\mathbf{x}+\mathbf{u}_{m-1}(\mathbf{x})) \tag{4}$$

where A^T denotes the transpose of A , and $\delta\mathbf{u}(x) = \mathbf{u}_m(x) - \mathbf{u}_{m-1}(x)$. This approximation is inserted into (3) to linearize this formulation:

$$\Phi^2 = \int_\Omega \left[f(\mathbf{x}) - g_u^m(\mathbf{x}) - \delta\mathbf{u}(\mathbf{x})^T\nabla g_u^m(\mathbf{x})\right]^2 \, dx \tag{5}$$

with $g_u^m(\mathbf{x}) = g(\mathbf{x} + \mathbf{u}_{m-1}(\mathbf{x}))$. This requires an interpolation of g at non-integer voxel positions. Here, a basic linear interpolation was used for the sake of simplicity. The term $(f(\mathbf{x}) - g_u^m(\mathbf{x}))$ is the correlation residual field (or discrepancy map). It is used as an indicator of the approximation quality of the displacement field $\mathbf{u}(\mathbf{x})$. If the convergence of the algorithm is reached, then $g_u^m(\mathbf{x}) \approx f(\mathbf{x})$ and one can approximate $\nabla g_u^m(\mathbf{x})$ by $\nabla f(\mathbf{x})$, which circumvents the gradient computation at every iteration. For determining $\nabla f(\mathbf{x})$, a centred finite difference approximation is used. The stationnarity condition associated with the minimization of (3), $\forall\delta\mathbf{u}^\star(\mathbf{x})$, reads:

$$\begin{aligned} &\int_\Omega \left[(\delta\mathbf{u}^\star(\mathbf{x}))^T\nabla f(\mathbf{x})\right] \, \left[\delta\mathbf{u}(\mathbf{x})^T\nabla f(\mathbf{x})\right] \, d\mathbf{x} = \\ &\int_\Omega \left[(\delta\mathbf{u}^\star(\mathbf{x}))^T\nabla f(\mathbf{x})\right] \, \left[f(\mathbf{x}) - g_u^m(\mathbf{x})\right] \, d\mathbf{x} \end{aligned} \tag{6}$$

The problem turns to find the best $\delta\mathbf{u}(\mathbf{x})$ that verifies (6). In a general approach, the unknown displacement field is interpolated as [5]:

$$\delta\mathbf{u}(\mathbf{x}) = \sum_n \mathbf{\Phi_n}(\mathbf{x}) q_n \tag{7}$$

where $\mathbf{\Phi_n}(\mathbf{x})$ are chosen basis functions and q_n the associated DOF. The problem consists then in determining the best q_n, which consequently determines the best $\delta\mathbf{u}(\mathbf{x})$ within the choice of the considered displacement fields.

Different choices are possible to specify the basis function $\mathbf{\Phi_n}(\mathbf{x})$, like piecewise polynomial (equivalent to sub-set approaches) [3], Fourier expansions [37], or precomputed numerical functions [19] for instance. Another choice consists in the shape functions [35, 5, 31] used in the finite element (FE) method. It ensures the continuity of the displacement field, which reduces measurement uncertainties [15]. In addition, it provides a direct link with numerical simulations, which can be of particular interest for identification and validation purposes [19, 2].

Remark: As shown later, when using a multigrid approach, the basis function may be adjusted for each iteration (different discretizations are used).

In this way, inserting (7) into (6), the following linear system must be solved at each iteration m of the DVC algorithm:

$$[M]\{\mathbf{q}\}_m = \{\mathbf{b}\}_m \tag{8}$$

with:

$$[M_{ab}] = \int_\Omega \left[\mathbf{\Phi_a}(\mathbf{x})^T \nabla \mathbf{f}\right] \left[\nabla \mathbf{f}^T \mathbf{\Phi_b}(\mathbf{x})\right] \, d\mathbf{x} \quad (9)$$

$$\{\mathbf{b_a}\}_m = \int_\Omega \left[\mathbf{\Phi_a}(\mathbf{x})^T \nabla \mathbf{f}\right] \left[f(\mathbf{x}) - g_u^m(\mathbf{x})\right] \, d\mathbf{x} \quad (10)$$

Since a Taylor expansion (equation (4)) is used , one has to solve system (8) iteratively for different values of the right-hand side (vector $\{b\}$) until convergence. Despite its advantages, the choice of FE shape functions ($\Phi_n(\mathbf{x})$ in (7)) may lead to the inversion of a set of linear systems (8) involving a high number of DOF. Consequently, the computational cost may become prohibitive. The following section presents a technique to integrate PGD with FE-based DVC, in order to speed-up (with appropriate accuracy) DVC measurements. It is based on the PGD-DIC method proposed in [27].

The PGD-DVC method

In this section, the basis of the PGD method and a detailed formulation of the integration of such an approach in the DVC are presented. A multigrid strategy and a regularization technique are also presented and included in the algorithm. The general structure of the PGD-DVC algorithm is then exposed.

Formulation

PGD uses a separated representation of a generic multidimensional function $F(x_1, x_2, ..., x_n)$. It consists in approximating this function by a finite sum of products involving low-dimensional functions:

$$F(x_1, x_2, ..., x_n) \approx \sum_{i=1}^{k} f_1^i(x_1) \cdot f_2^i(x_2) \cdot ... \cdot f_n^i(x_n) \quad (11)$$

The separated dimensions can be, for instance, space and time variables [18], deterministic and stochastic variables [23], space variables and parameters [29], but also different dimensions of space independently [6, 27]. Here, extending the work of [27] to DVC measurements, the unknown displacement field $\mathbf{u}(x, y, z)$ is written in a separated form for each of its components (u, v, w) using unidimensional functions only:

$$\begin{aligned} \mathbf{u}(x,y,z) &= \begin{pmatrix} u(x,y,z) \\ v(x,y,z) \\ w(x,y,z) \end{pmatrix} \\ &\approx \sum_{i=1}^{m} \begin{pmatrix} u_i^x(x) \cdot u_i^y(y) \cdot u_i^z(z) \\ v_i^x(x) \cdot v_i^y(y) \cdot v_i^z(z) \\ w_i^x(x) \cdot w_i^y(y) \cdot w_i^z(z) \end{pmatrix} \end{aligned} \quad (12)$$

where the functions $u_i^x, u_i^y, u_i^z, v_i^x, v_i^y, v_i^z, w_i^x, w_i^y, w_i^z$ are unknown a priori. These functions are obtained with a fixed point algorithm (power type method [23]) . At iteration m of the DVC algorithm, the displacement field is decomposed as:

$$\begin{aligned} \mathbf{u}(x,y,z) = &\underbrace{\sum_{i=1}^{m-1} \begin{pmatrix} u_i^x(x) \cdot u_i^y(y) \cdot u_i^z(z) \\ v_i^x(x) \cdot v_i^y(y) \cdot v_i^z(z) \\ w_i^x(x) \cdot w_i^y(y) \cdot w_i^z(z) \end{pmatrix}}_{\mathbf{u}_{m-1}(x,y,z)} \\ &+ \underbrace{\begin{pmatrix} u_m^x(x) \cdot u_m^y(y) \cdot u_m^z(z) \\ v_m^x(x) \cdot v_m^y(y) \cdot v_m^z(z) \\ w_m^x(x) \cdot w_m^y(y) \cdot w_m^z(z) \end{pmatrix}}_{\delta\mathbf{u}(x,y,z)} \end{aligned} \quad (13)$$

where $\mathbf{u}_{m-1}$ collects the terms calculated by all the previous iterations, and $\delta\mathbf{u}$ is composed of the unknown functions at the present iteration m. By using this formulation, the best correction $\mathbf{u}_m - \mathbf{u}_{m-1}$ minimizes the least square formulation associated with the brightness conservation (1).

Remark: Such a tensor decomposition is more likely to handle parallelepipedic ROI shapes. However, as shown in [26], there are no theoretical limitations for the use of arbitrary shapes.

By using this approach, $\mathbf{u}_{m-1}(x, y, z)$ is considered fixed, whereas the set of 9 functions $u_m^x, u_m^y, u_m^z, v_m^x, v_m^y, v_m^z, w_m^x, w_m^y, w_m^z$ are unknown. The corresponding test field is classically assumed to be written as [27, 29]:

$$\delta\mathbf{u}^\star = \begin{pmatrix} u_m^{x_\star}\cdot u_m^y\cdot u_m^z + u_m^x\cdot u_m^{y_\star}\cdot u_m^z + u_m^x\cdot u_m^y\cdot u_m^{z_\star} \\ v_m^{x_\star}\cdot v_m^y\cdot v_m^z + v_m^x\cdot v_m^{y_\star}\cdot v_m^z + v_m^x\cdot v_m^y\cdot v_m^{z_\star} \\ w_m^{x_\star}\cdot w_m^y\cdot w_m^z + w_m^x\cdot w_m^{y_\star}\cdot w_m^z + w_m^x\cdot w_m^y\cdot w_m^{z_\star} \end{pmatrix} \tag{14}$$

Inserting $\delta\mathbf{u}^\star$ and $\delta\mathbf{u}$ in problem (6) leads to a nonlinear system composed of nine coupled variational formulations. By gathering the unknown functions depending on the same dimension, one can write (6) as 3 coupled linear problems:

$$\int_z \gamma^{\star T}\,\mathbf{A}(z)\gamma\,dz = \int_z \gamma^{\star T}\,\mathbf{B}(z)\,dz \tag{15}$$

$$\int_y \beta^{\star T}\,\mathbf{C}(y)\beta\,dy = \int_y \beta^{\star T}\,\mathbf{D}(y)\,dy \tag{16}$$

$$\int_x \alpha^{\star T}\,\mathbf{E}(x)\alpha\,dx = \int_x \alpha^{\star T}\,\mathbf{F}(x)\,dx \tag{17}$$

with

$$\gamma = \begin{bmatrix} u_m^z \\ v_m^z \\ w_m^z \end{bmatrix} \quad \beta = \begin{bmatrix} u_m^y \\ v_m^y \\ w_m^y \end{bmatrix} \quad \alpha = \begin{bmatrix} u_m^x \\ v_m^x \\ w_m^x \end{bmatrix}$$

where $\mathbf{A}(z), \mathbf{B}(z), \mathbf{C}(y), \mathbf{D}(y), \mathbf{E}(x), \mathbf{F}(x)$ are, respectively, three symmetric operators and three vectors composed of only one-dimensional coefficients. For instance, $\mathbf{A}(z)$ and $\mathbf{B}(z)$ writes:

$$\mathbf{A}(z) = \begin{bmatrix} A_{11}(z) & A_{12}(z) & A_{13}(z) \\ A_{12}(z) & A_{22}(z) & A_{23}(z) \\ A_{13}(z) & A_{23}(z) & A_{33}(z) \end{bmatrix}; \mathbf{B}(z) = \begin{bmatrix} B_1(z) \\ B_2(z) \\ B_3(z) \end{bmatrix}$$

and

$$\begin{aligned} A_{11} &= \int_x (u_m^x)^2 \int_y (u_m^y \frac{\partial f}{\partial x})^2\,dydx \\ A_{12} &= \int_x u_m^x\,v_m^x \int_y u_m^y\,v_m^y \frac{\partial f}{\partial x}\,\frac{\partial f}{\partial y}\,dydx \\ A_{13} &= \int_x u_m^x\,w_m^x \int_y u_m^y\,w_m^y \frac{\partial f}{\partial x}\,\frac{\partial f}{\partial z}\,dydx \\ B_1 &= \int_x u_m^x \int_y u_m^y\,(f-g_u)\,\frac{\partial f}{\partial x}\,dydx \\ B_2 &= \int_x v_m^x \int_y v_m^y\,(f-g_u)\,\frac{\partial f}{\partial y}\,dydx \\ B_3 &= \int_x w_m^x \int_y w_m^y\,(f-g_u)\,\frac{\partial f}{\partial z}\,dydx \end{aligned}$$

Similarly, the group of coefficients $\mathbf{C}(y), \mathbf{D}(y), \mathbf{E}(x), \mathbf{F}(x)$ are only one-dimensional operators. By applying an alternating directions fixed point algorithm, one can compute the group of functions (γ, β, α). It consists in, firstly, supposing β and α fixed, so that $\beta^\star$ and $\alpha^\star$ vanishes. Consequently, the system (15)-(17) reduces to a problem involving only the z dimension (equation (15)).

One should notice that the linear formulation of the correlation problem has become nonlinear (system (15)-(17)). However, it is convenient because a problem of cubic complexity (or quadratic in 2D problems) is substituted by various problems of linear complexity. It can be solved by any numerical method, as finite elements, which needs only 1D mesh in this case. Then, the unknown vector field $\gamma(z)$ is written as:

$$\gamma = \begin{pmatrix} \sum_{j=1}^n N_j(z)a_j \\ \sum_{j=1}^n N_j(z)b_j \\ \sum_{j=1}^n N_j(z)c_j \end{pmatrix} = \mathbf{N}^z\,q_\gamma \tag{18}$$

where $\mathbf{N}^z$ is a matrix collecting all the FE shape functions and q_γ the associated DOF vector.

Remark: By using this PGD approach, only 1D meshes in each direction are needed. Then, the total number of DOF involved (DOF_{PGD}) is lower than that obtained with a FE-based approach (DOF_{FE}), for a same elements size:

$$\begin{aligned} DOF_{PGD} &= 3\cdot(n_x + n_y + n_z) \\ DOF_{FE} &= 3\cdot(n_x\cdot n_y\cdot n_z) \end{aligned} \tag{19}$$

where n is the number of nodes in each direction.

By inserting (18) into (15), the following linear system is obtained:

$$\mathbb{A}\ q_\gamma = \mathbb{B} \tag{20}$$

with

$$\mathbb{A} = \int_z (\mathbf{N}^z)^T \mathbf{A}(z) \mathbf{N}^z\ dz \qquad \mathbb{B} = \int_z (\mathbf{N}^z)^T \mathbf{B}(z)\ dz$$

Similarly to the z dimension problem, this procedure is made for the other two dimensions (x and y). Then, the fixed point algorithm consists in solving three linear systems (corresponding to each dimension, see (20)), which must be repeated until convergence. The following criterion of stagnation is used [27]:

$$\eta_f^2 = \frac{\|\gamma_k - \gamma_{k-1}\|^2}{\|\gamma_k\|^2} + \frac{\|\beta_k - \beta_{k-1}\|^2}{\|\beta_k\|^2} + \frac{\|\alpha_k - \alpha_{k-1}\|^2}{\|\alpha_k\|^2} < \epsilon_f \tag{21}$$

where $\|\cdot\|$ is the Eucledian norm, k is the current iteration of the fixed point algorithm, and ϵ_f is a user-specified convergence parameter. The choice of ϵ_f and the maximum number of fixed point iterations k_{max} are discussed in section 5.3.

It is important to notice that the fixed point algorithm is a step inside the global correlation algorithm. Following [27], the proposed PGD-DVC algorithm computes only one best rank-one approximation at each nonlinear update of $g(\mathbf{x} + \mathbf{u}(\mathbf{x}))$, associated with the correlation iterations. Specifically, each approximation of the fixed point algorithm will provide new functions $u^x, u^y, u^z, v^x, v^y, v^z, w^x, w^y, w^z$ used to correct the displacement field $\mathbf{u}_{m-1}$ (see equation (13)).

By using rank-one approximations, the total number of correlation iterations is dependent on the separability of the unknown field. However, as shown in [27], when a high number of modes are necessary for approximating a hardly separable field, the PGD approach still allows for a reduction of the CPU time (compared to a FE approach).

To measure the convergence of the correlation problem, the following stagnation indicator (based on the relative norm of each 3D field correction component) is introduced [27]:

$$\eta_c^2 = \frac{\|\delta\mathbf{u}\|^2}{\|\mathbf{u}\|^2} + \frac{\|\delta\mathrm{v}\|^2}{\|\mathrm{v}\|^2} + \frac{\|\delta\mathrm{w}\|^2}{\|\mathrm{w}\|^2} < \epsilon_c \tag{22}$$

where $\|\cdot\|$ is the Eucledian norm and ϵ_c is a user-specified convergence parameter of the correlation problem. The accuracy of the converged displacement field can also be assessed by the stagnation of a norm of the correlation residual field (discrepancy map).

Multigrid PGD

The use of a Taylor expansion for the linearization process of the correlation problem (4), requires a low ratio between the displacement ($\delta\mathbf{u}(\mathbf{x})$) and the spatial variations of the image gray levels ∇g_u. Then, large displacements with a poor texture may lead to a non-convergence of the correlation algorithm. To circumvent this issue, a coarse graining strategy is usually used [5, 33, 14]. It relies on one or more coarser grids to enlarge the mesh size and smooth the texture, which decreases the ratio displacement/texture. Then, $\delta\mathbf{u}(\mathbf{x})$ remains small and a Taylor expansion can be applied, increasing the maximum measurable displacement obtained with conventional DIC/DVC techniques [14].

In this way, a multigrid version of the PGD approach proposed in [27] is developed. Indeed, thanks to its additive nature, PGD can use different grids for each term in the decomposition. Thus the multigrid-PGD approximation reads:

$$\begin{aligned}\mathbf{u}(x,y,z) \approx & \underbrace{\sum_i \begin{pmatrix} u_i^x(x)\cdot u_i^y(y)\cdot u_i^z(z) \\ v_i^x(x)\cdot v_i^y(y)\cdot v_i^z(z) \\ w_i^x(x)\cdot w_i^y(y)\cdot w_i^z(z) \end{pmatrix}}_{1^{st}\text{ grid}} + \dots \\ & + \underbrace{\sum_i \begin{pmatrix} u_i^x(x)\cdot u_i^y(y)\cdot u_i^z(z) \\ v_i^x(x)\cdot v_i^y(y)\cdot v_i^z(z) \\ w_i^x(x)\cdot w_i^y(y)\cdot w_i^z(z) \end{pmatrix}}_{h^{th}\text{ grid}}\end{aligned} \tag{23}$$

Initially, large elements are used along each axis, and then the unidimensional meshes are refined during convergence. This multigrid PGD is associated to the above coarse graining strategy applied to the images.

The general form of the algorithm can be visualized

```
Initialization: create coarser images;
for h ← h_max to 0 do
    Mesh coarse image;
    if h = h_max then
        Rigid body translation;
        → [γ, β, α]_o;
    else
        Interpolation using [γ, β, α]_{h+1};
        → [γ, β, α]_o;
    end
    Correlation solver: [γ, β, α]_o → [γ, β, α]_h;
    Fill [γ, β, α]_{h−1} with [γ, β, α]_h;
end
[γ, β, α]_o = [γ, β, α]_h;
```

Figure 1: The PGD-based multigrid algorithm. Each coarser level h computes a new solution, used at the next level $h-1$.

in Figure 1. First, coarser images of the reference image are generated for each level $h = 0, 1, ..., h_{max}$, in order to smooth the texture of the images. At each level, the original size of the ROI is divided by 2^h. The new image is coarse-textured by combining groups of $2 \times 2 \times 2$ voxels into a single voxel (by using the mean value of gray-levels in each direction) so the number of voxels per element remains constant at each level. Then, starting from coarser level h_{max}, three first unidimensional meshes are generated (one for each dimension). At this first stage a rigid body translation is used as a primarily initialization. For all the other levels, three new unidimensional meshes are generated (one for each dimension) and the mesh is refined by 2 with respect to the previous grid. After convergence, the algorithm yields a multiscale solution that is expressed on multiple grids. These grids may have nonconforming discretizations (different nodes positions). Note that the grids exchange information directly through the images, avoiding the need of projection or intergrid operations [30].

A representation of coarser images and their meshes is demonstrated in Figure 2, using 4 coarsening levels. In sections 4 and 5 the proposed strategy is applied to synthetic and real examples, in order to present its effect to the convergence of the correlation problem.

Regularization

The determination of the optical flow (1) is an ill-posed problem. Then, there is no unique motion explaining an image brightness change [22, 16]. In this way, a regularization process integrated to each scale of the multigrid correlation problem may be advantageous to reach lower residuals. Following [16], a spatial constraint (or smooth constraint) is introduced in the global least square approach (3):

$$\Phi^2_{reg} = \Phi^2 + \lambda\, \Phi^2_L \tag{24}$$

The parameter λ weights the influence of the regularization on the correlation problem. The general idea is to smooth the displacement field, which can be based on the Laplace operator:

$$\Phi^2_L = \int_{\mathbf{x}} \left(\frac{d\mathbf{u}(\mathbf{x})}{dx}^2 + \frac{d\mathbf{u}(\mathbf{x})}{dy}^2 + \frac{d\mathbf{u}(\mathbf{x})}{dz}^2 \right) d\mathbf{x} \tag{25}$$

For this paper, λ was chosen empirically, based on the residuals of the correlation problem. The use of a regularized formulation allows the use of smaller elements size, which may improve the spatial resolution. It will be discussed later, in section 5.2. For more details of the regularization formulation using a PGD approach, readers may refer to [27].

A representation of the general PGD-DVC algorithm is presented in Figure 3 (m_{max} is chosen by the user, in order to avoid infinite iterations when the convergence is not possible). In this work, a Matlab code with C++ subroutines was developed. In the next section the proposed method is validated by using artificial images. The results are compared with a standard FE-based DVC, considered as reference.

Validation using an artificial example

In this section, an a priori performance of the PGD-DVC method is analyzed and compared to a FE-based DVC, using eight-noded hexahedron elements, considered as reference. Additionally, the effect of the multigrid strategy to the convergence of the correlation problem is analyzed. For these purposes, an artificial reference image of $150 \times 150 \times 150$ voxels was built based on an

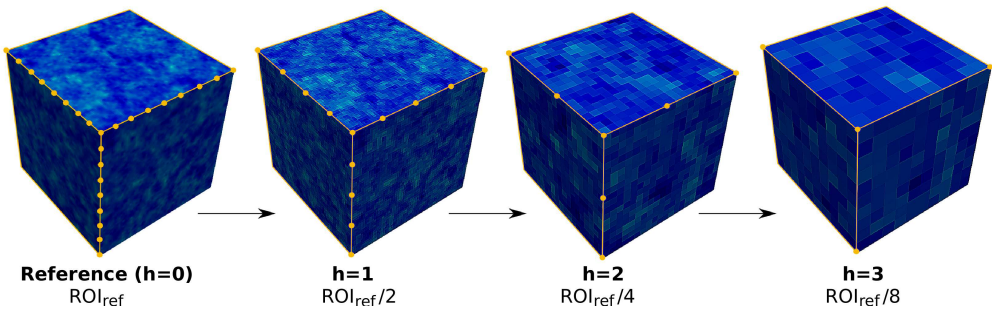

Figure 2: Representation of the PGD-based multigrid coarse images, with a reference ROI of $80 \times 80 \times 80$ voxels and element length of 10 voxels in each direction (using 4 coarsening levels).

extension to 3D of a Perlin noise [28]. The generated image is shown in Figure 4a, and the histogram of gray levels in Figure 4b. The image has 8-bit depth, the mean value of gray levels is ≈ 128 gray levels, the typical size of patterns are $\approx 3,2$ voxels and the standard deviation ≈ 18 gray levels. The 2D procedure for generating an artificial image is described in details in [24].

Noise sensitivity

Firstly, to investigate the displacement resolution, a noise sensitivity analysis is performed [5]. It consists in adding a random noise with a standard deviation of $\sigma_n = 1$ gray levels at each voxel of a reference image f, generating a new image g. It represents the noise associated with the image acquisition [20]. Then, the DVC algorithm is applied using this pair of images. The estimated displacement field is expected to be zero, since no displacement field is introduced on the image. Following [20], the standard displacement uncertainty σ_u is such that:

$$\sigma_u \propto \frac{\sigma_n}{L^{3/2}} \tag{26}$$

where L is the number of voxels in the considered element. The standard displacement uncertainty σ_u (considering the voxels over the entire ROI) as a function of the element size can be viewed in Figure 5. The interpolation line is described by a power law A/L^{α}, where $\alpha = 1.76$ is in good agreement with equation (26).

Sub-pixel interpolation sensitivity

Additionally, another indicator was used to analyze the uncertainty of PGD-DVC measurements. It consists in generating a sequence of translated images g_i from the reference image f by an imposed displacement u_{ref} (without noise) , as proposed by [5]. A translation was interpolated linearly in the y-direction, with u^p_{ref} taking the values $p = \{0.1, 0.2, ..., 1\}$ pixel, as sub-pixels interpolations are the main source of errors [5]. The quality of the measured displacement (u^p_m) of u^p_{ref} can be assessed by the standard displacement uncertainty σ_u, and the mean displacement error δ_u, defined by:

$$\langle \sigma_u \rangle_s = \frac{1}{10} \sum_{p=0.1}^{1} \langle (u^p_m - \langle u^p_m \rangle)^2 \rangle^{1/2} \tag{27}$$

$$\langle \delta_u \rangle_s = \frac{1}{10} \sum_{p=0.1}^{1} |\langle u^p_m \rangle - u^p_{ref}| \tag{28}$$

where $\langle u \rangle$ defines the mean value of a displacement field u over each voxel of the ROI and $\langle \cdot \rangle_s$ the average over the 10 shift values . Figure 6 shows $\langle \sigma_u \rangle_s$ and $\langle \delta_u \rangle_s$ as a function of the element size. The displacement uncertainty decreases when the element size increases, as expected [20, 5, 32]. The results also reveal that the PGD-DVC method is in good agreement with FE-DVC regarding measurement quality. Finally, one can observe that for large element sizes (higher than 80 voxels in each direction, in this case) the uncertainties increase, which is justified by a poor statistical information (only one

Load f and g images;
ROI definition and mesh;
Compute gradient (∇f);
Multigrid solutions (u_o);
Regularization operator construction;

$\Longrightarrow$ CORRELATION ITERATIONS;
Initialization: $m = 1$;
while ($\eta_c > \epsilon_c$) and ($m < m_{max}$) do
  Update residual $f - g_u$;

  $\Longrightarrow$ FIXED POINT ALGORITHM;
  Initialization: $[\gamma, \beta, \alpha]$; $k = 1$;
  while ($\eta_f > \epsilon_f$) and ($k < k_{max}$) do
    (β, α) fixed: z-monodimensional problem;
    $\rightarrow$ Compute γ;
    (γ, α) fixed: y-monodimensional problem;
    $\rightarrow$ Compute β;
    (γ, β) fixed: x-monodimensional problem;
    $\rightarrow$ Compute α;
    Fixed point stagnation indicator η_f;
    $k = k + 1$;
  end
  Convergence indicator η_c;
  Displacement update:
  $u_o = u_o + \begin{pmatrix} u_m^x \cdot u_m^y \cdot u_m^z \\ v_m^x \cdot v_m^y \cdot v_m^z \\ w_m^x \cdot w_m^y \cdot w_m^z \end{pmatrix}$;
  $m = m + 1$;
end

Figure 3: The PGD-DVC algorithm. A fixed point algorithm (which involves only uni-dimensional problems) is integrated into the correlation iterations.

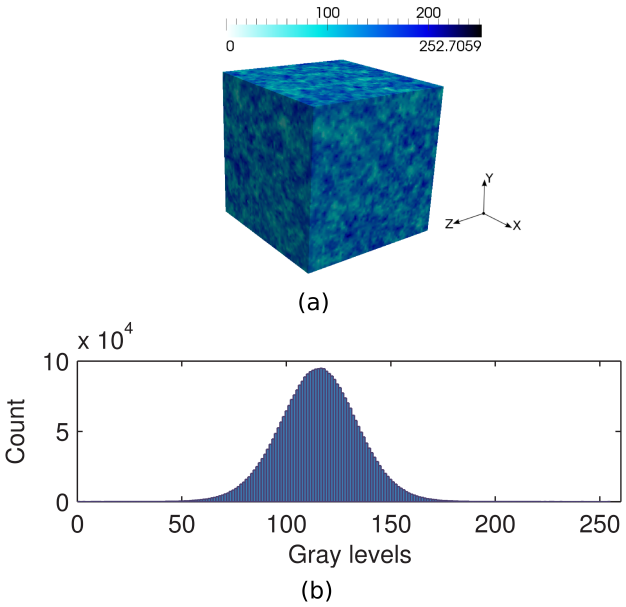

Figure 4: (a) Artificial reference image f based on Perlin noise. Mean value ≈ 128 gray levels, standard deviation ≈ 18 gray levels ; (b) Histogram of gray levels.

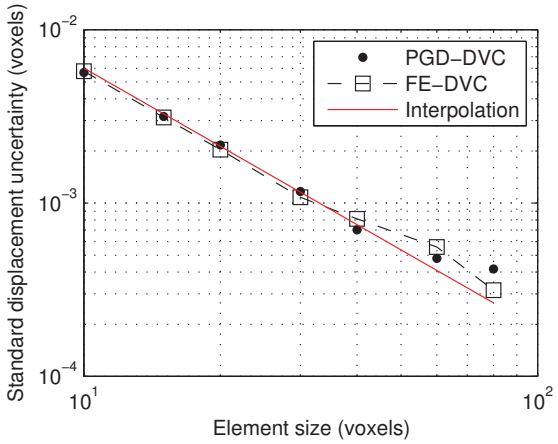

Figure 5: Noise sensitivity analysis. σ_u as a function of element size, for both methods.

element in each direction in this case) .

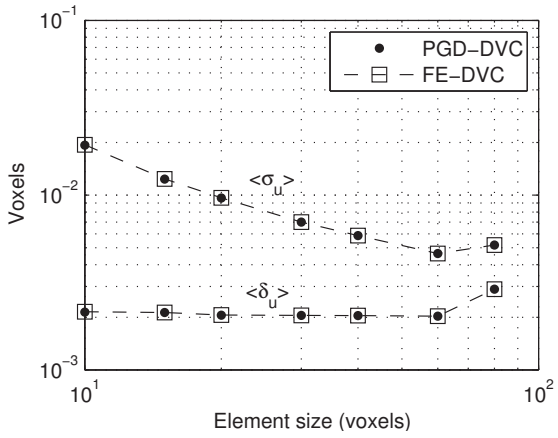

Figure 6: Sub-pixel interpolation sensitivity. $\langle\sigma_u\rangle_s$ and $\langle\delta_u\rangle_s$ as a function of element sizes, for both methods.

A first synthetic example

Last, a more complex displacement is imposed in order to compare the measured displacement field obtained by both methods. By using spherical coordinates, each component of the imposed displacement field is written as:

$$\begin{aligned}\mathbf{u}_{imp}(r,\theta,\phi) &= \begin{pmatrix} u(r,\theta,\phi) \\ v(r,\theta,\phi) \\ w(r,\theta,\phi) \end{pmatrix} \\ &= \begin{pmatrix} r^4\left[a.cos(\theta) - b.sin(\phi)\right] \\ r^4\left[a.sin(\theta) - b.cos(\phi)\right] \\ r^4\left[a.cos(\theta) - b.cos(\phi)\right] \end{pmatrix}\end{aligned} \tag{29}$$

where a and b are weight parameters. The components of the imposed displacement field are functions of all the three spatial dimensions. Consequently, the decomposition by PGD of such field is nontrivial. The reference image used here is the same as the one presented in Figure 4a. The x- component of the prescribed displacement field is shown in Figure 7 (in this particular case, $a = 2$ and $b = 5$). The chosen ROI has $120 \times 120 \times 120$ voxels, and the elements size is set to 20 voxels in each direction.

The difference (residual) between the imposed and the measured $x-$ component of the displacement field (U_x^{ref} and $U_x^{PGD/FE}$, respectively), and the discrepancy map (with respect to the dynamic range) obtained for both methods are presented in Figure 8. The mean value and standard deviation corresponding to Figure 8a and 8b are $\approx 1.6 \cdot 10^{-3}$ and ≈ 0.03, respectively. For Figure 8c and 8d, the mean value and standard deviation are $\approx 2.10^{-14}\%$ and $\approx 1.7\%$, respectively. The PGD-DVC algorithm converged with $m = 62$ iterations (using $\epsilon_c = 10^{-3}$). One can observe that the measured displacement field obtained by PGD-DVC is very close to the one measured with FE-DVC.

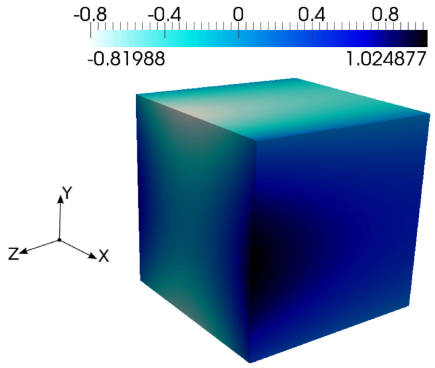

Figure 7: x- component of the prescribed displacement field (voxels).

Effects of the multigrid strategy

To exemplify the use of a multigrid strategy, a more important displacement field (≈ 30 voxels of magnitude in the y- direction) utilizing (29) was imposed to the same reference image (Figure 4a). Elements size of 20 voxels in each direction was used, with a ROI of $80 \times 80 \times 80$ voxels.

Following [33], Figure 9a shows that when only one single grid is used without regularization, the convergence of the correlation problem is not obtained (in this case, $\epsilon_c = 10^{-3}$). When using three grids (without regularization), the convergence is reached and the measurement can be performed.

Additionally, Figure 9b shows that when no multigrid nor regularization are used, the choice of the elements size is restricted. Then, reaching lower residuals is only possible when using both numerical strategies. These

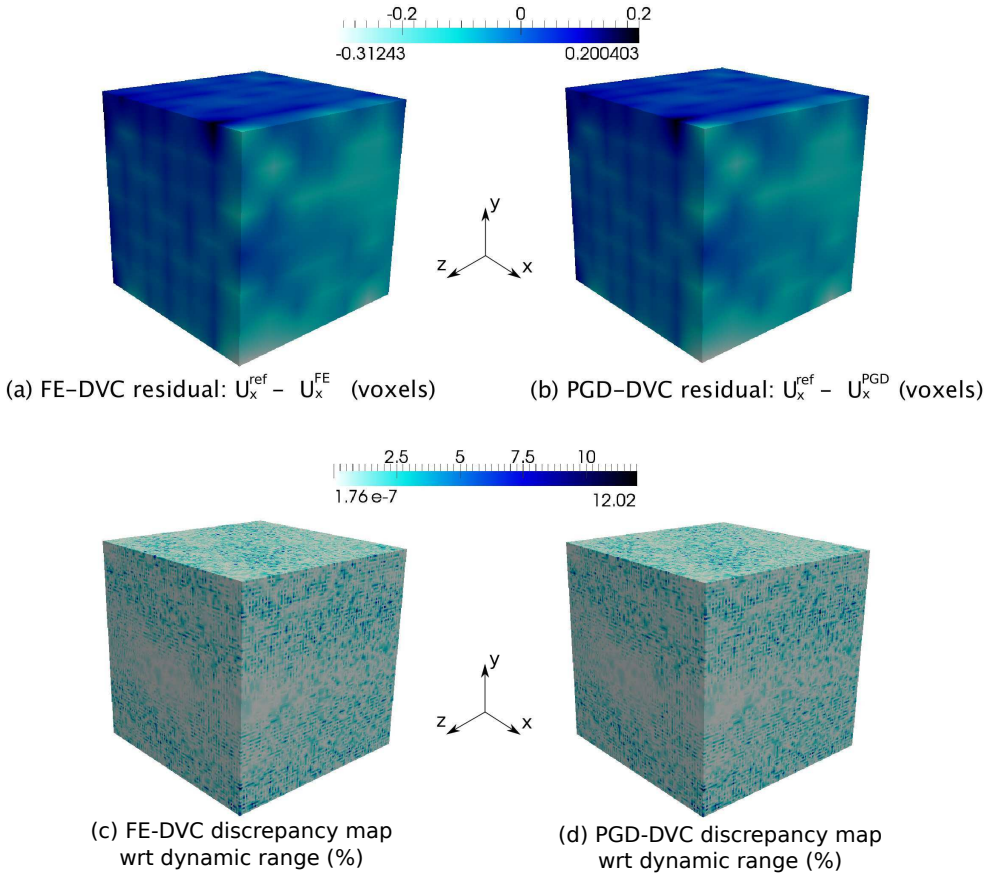

Figure 8: Artificial example. Measurements results for FE-DVC and PGD-DVC. (a) and (b) Residual between the imposed and the measured $x-$ component of the displacement field (U_x^{ref} and $U_x^{PGD/FE}$, respectively). Mean value $\approx 1.6 \cdot 10^{-3}$, standard deviation ≈ 0.03 ; (c) and (d) Discrepancy map with respect to the dynamic range (mean value $\approx 2.10^{-14}\%$, standard deviation $\approx 1.7\%$ for both methods).

results show that a combination of multigrid and regularization makes the algorithm more robust to large displacement fields and/or fine grids.

Application to a real experiment: trabecular bone compression

In this section, a real example of a trabecular bovine bone under compression, monitored by micro-MRI, is studied. This case was firstly analyzed in [4], using a FE-based DVC algorithm (with eight-noded hexahedron elements) to determine the displacement and strain fields. The data can be useful for FE models validation and also to determine the material properties.

The experiment consists in compressing a bovine bone specimen. Its natural trabecular network is used as a texture for DVC. The field of view of the MRI images is $256 \times 512 \times 256$ voxels, corresponding to 40mm x 20mm x 20mm . For a detailed description of the specimen preparation, compression device and image acquisition, readers may refer to [4].

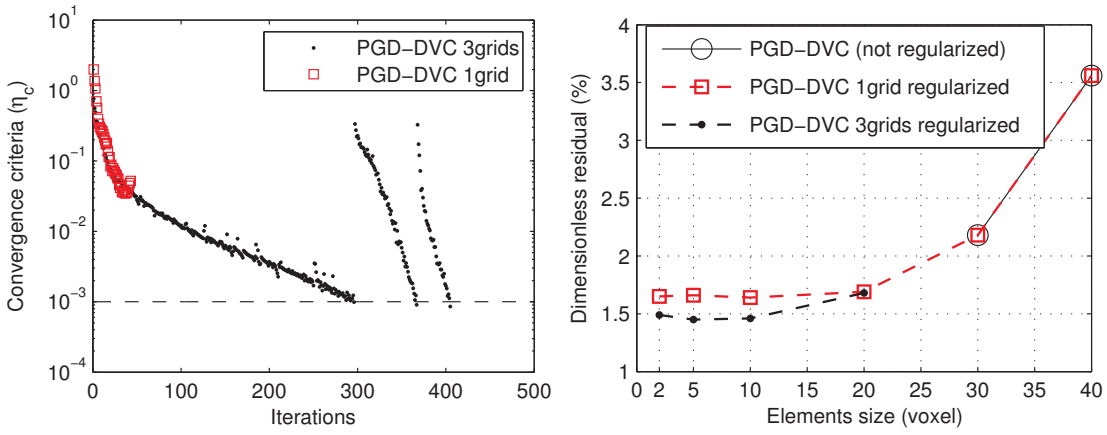

(a) (b)

Figure 9: Analysis of the PGD multigrid and regularization, applied to a pair of synthetic volumetric images with a large imposed displacement field. (a) Convergence criteria during the correlation iterations m . The use of different grids (without regularization) allowed the convergence of the correlation problem (elements size = 20 voxels); and (b) Dimensionless residual as a function of the elements size. The use of the multigrid strategy combined with regularization allows to achieve lower residuals.

A priori analysis

Here, a comparison is made between PGD-DVC and FE-DVC performances (considered as reference). The chosen ROI is composed of $95 \times 180 \times 100$ voxels , in order to enclose the maximum of the specimen (which has the dimension of 16mm x 10mm x 10mm) . The reference image (corresponding to the chosen ROI) is shown in Figure 10a (standard deviation ≈ 24 gray levels, size of patterns $\approx 2,2$ voxels) . One can observe its natural texture, necessary for the DVC correlation problem. The standard displacement uncertainty $\langle \sigma_u \rangle_s$ and the mean displacement error $\langle \delta_u \rangle_s$ (without noise) , as a function of the elements size are shown in Figure 10b. The results show that measured displacements have a subvoxel resolution, which is in good agreement with [4].

Displacement Measurements

The measured displacement field and the associated discrepancy map (with respect to the dynamic range) obtained by each technique (using the same ROI as shown in Figure 10a) are presented in Figure 11, using element size of 20 voxels in each direction. The mean displacement $\langle U_y \rangle$ is equal to $\approx -4,5$ voxels, which is is accordance with [4]. The mean value and the standard deviation of the difference (residual) between the measured displacement field in the y-direction $U_y^{FE} - U_y^{PGD}$ (Figure 11c) are, respectively, $\approx 3.6 \cdot 10^{-4}$ and ≈ 0.013 voxels. The measured displacement fields and discrepancy maps of both methods are very similar. The PGD-DVC algorithm converged after 39 iterations m (with $\epsilon_c = 10^{-3}$).

Figure 12a shows that, when using elements size of 15 voxels without regularization, the convergence of the correlation problem is only reached when using the multigrid strategy (three grids in this case). In Figure 12b, the use of smaller elements size allows to reach lower correlation residuals, which is possible when combining regularization with multigrid. However, smaller elements size increases the number of DOF, which may lead to prohibitive computational costs. In this way, a CPU time analysis is performed, in order to compare the computational cost of the proposed method with that of FE-based DVC.

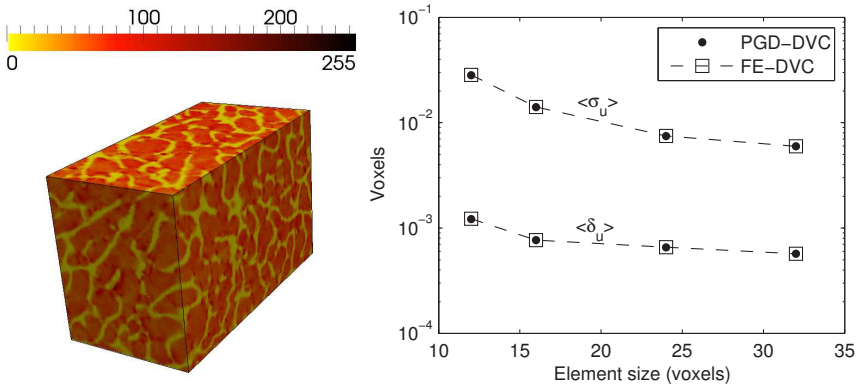

(a) (b)

Figure 10: Practical case primary analysis. (a) reference image (gray levels) of the trabecular bone, obtained by micro-MRI. The ROI is composed of $95 \times 180 \times 100$ voxels , standard deviation ≈ 24 gray levels ; and (b) Uncertainty analysis: $\langle \sigma_u \rangle_s$ and $\langle \delta_u \rangle_s$, associated with imposed sub-voxel displacements.

CPU time analysis

As demonstrated in [27], the computational cost obtained with the proposed method may become significantly lower than the one associated to a FE-based DIC/DVC, especially when small elements are used to improve the resolution. Figure 13a shows the CPU time as a function of the elements size . The same initialization (one grid only, rigid body translation), regularization and ROI size ($95 \times 180 \times 100$ voxels) were used for both methods. When perfoming measures with fine spatial resolution, the computational cost of PGD-DVC is much lower than FE-DVC.

Figure 13b shows the CPU time as a function of k_{max}, the maximum number of fixed-point algorithm iterations (see Figure 3), specified by the user. The same ROI ($95 \times 180 \times 100$ voxels) , elements size (10 voxels) and convergence criterion of the correlation problem η_c (10^{-3}) were used. Solving the fixed-point accurately (choosing a large k_{max}) leads to inefficient iterations, which unnecessarily increase the computational cost without improving the accuracy nor the convergence rate of the correlation solver. Conversely, performing only one fixed point iteration ($k_{max} = 1$) induces a high increase of the number of iterations m of the correlation problem, increasing the CPU time. One can observe that, in this example, few iterations k are necessary (more precisely, from two to five iterations) to obtain accurate results with a minimum computational cost.

Summary and conclusions

In this article, an extension of the PGD-based digital image correlation (PGD-DIC) to volumetric displacement measurements (PGD-DVC) is presented. The idea consists in seeking the unknown 3D displacement field as a product of separated 1D spatial functions. Each problem is solved independently thanks to a fixed-point algorithm, which reduces the numerical complexity. Results show that very few iterations of the fixed-point and one single best rank one approximation at each linear prediction of the correlation are necessary for the convergence of the correlation problem.

Additionally, a multigrid PGD was developed which allows to handle meshes defined at different scales in the decomposition. Associated to image coarse graining [5, 33], this method improves the convergence of the standard PGD-DIC [27] by avoiding local minima. This is the case, for instance, when displacements are large when compared to the gray level spatial variations of the images . This multigrid PGD allows to reach a bet-

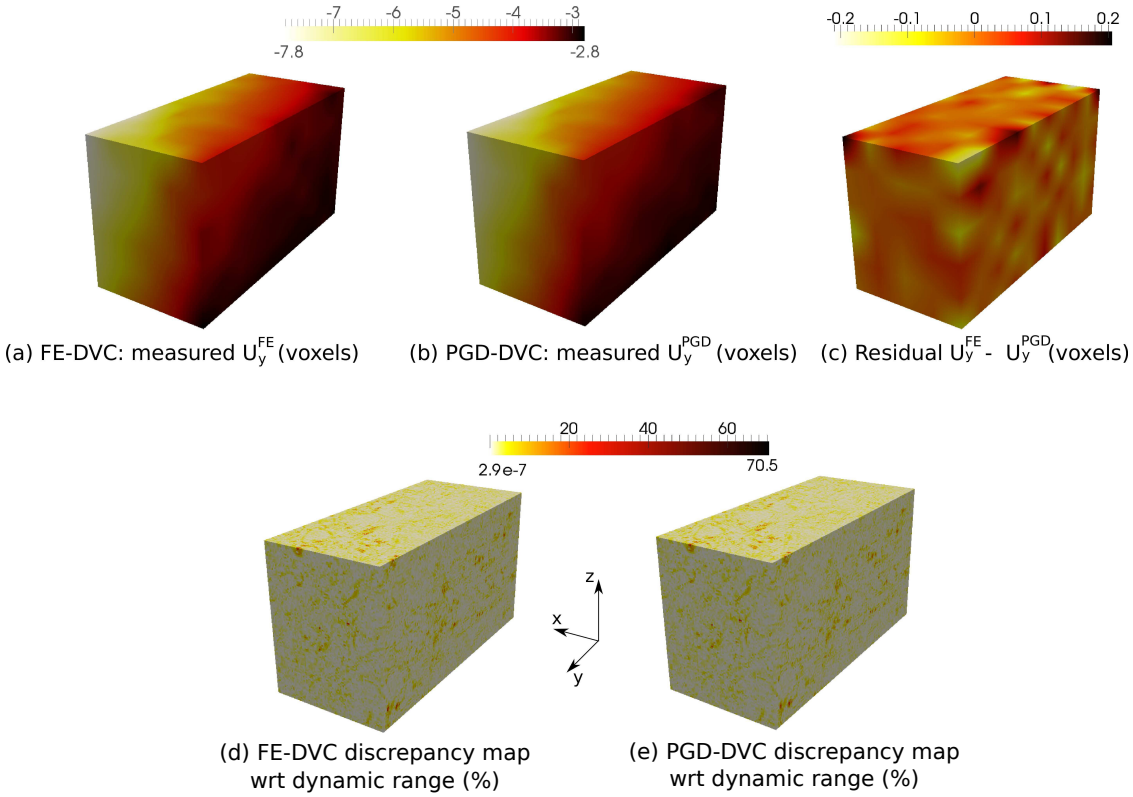

Figure 11: Practical case results, for both methods. (a) and (b) y- component of the displacement field; (c) Difference between measurements U_y^{FE} and U_y^{PGD} (mean value: $\approx 3.6 \cdot 10^{-4}$ voxels, standard deviation: ≈ 0.013 voxels); (d) and (e) Discrepancy map with respect to the dynamic range (mean value $\approx 5.10^{-13}\%$, standard deviation $= 2.5\%$ for both methods).

ter matching between the reference and deformed image whether a regularization technique is used or not.

When compared with a standard FE-based DVC, using artificial and practical cases, the proposed method has the same performance regarding uncertainty analysis. Both methods produce very similar results , since the interpolation should theoretically span the same approximation space. By decreasing the element size to obtain a finer spatial resolution , the proposed method admits a reduced computational cost compared to FE-based DVC.

The use of very large ROI sizes leads to additional challenges associated with the computational cost. For instance, a ROI composed of $2000 \times 2000 \times 2000$ voxels may result in more than 10^6 DOF, when using relatively large element size of 20 voxels. Consequently, PGD-DVC should represent an adequate and efficient method to deal with measurements and identification of constitutive laws at the voxel-scale [20, 10].

Acknowledgments

This work was funded by the Ministry of Higher Education and Research (MESR) along with AAP01 Research project 2013 University of Toulouse III (Composcope Project). The experimental data were obtained with the help of A. Benoit, S. Guérard, B. Gillet, G. Guillot, F. Hild, D. Mitton, and S. Roux, to whom the authors are grateful. Last the authors would like to thank the anony-

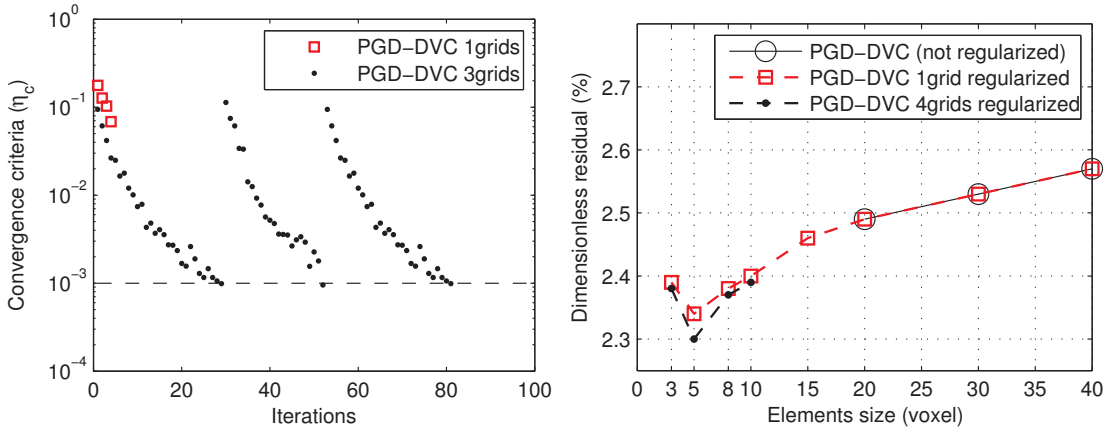

Figure 12: Analysis of the PGD multigrid and regularization, applied to micro-MRI images of a trabecular bone under compression. (a) Convergence criteria during the correlation iterations m. The use of multigrid (without regularization) allowed the convergence of the correlation problem (elements size = 15 voxels); and (b) Dimensionless residual as a function of the elements size. The use of the multigrid strategy combined with regularization allows to achieve lower residuals.

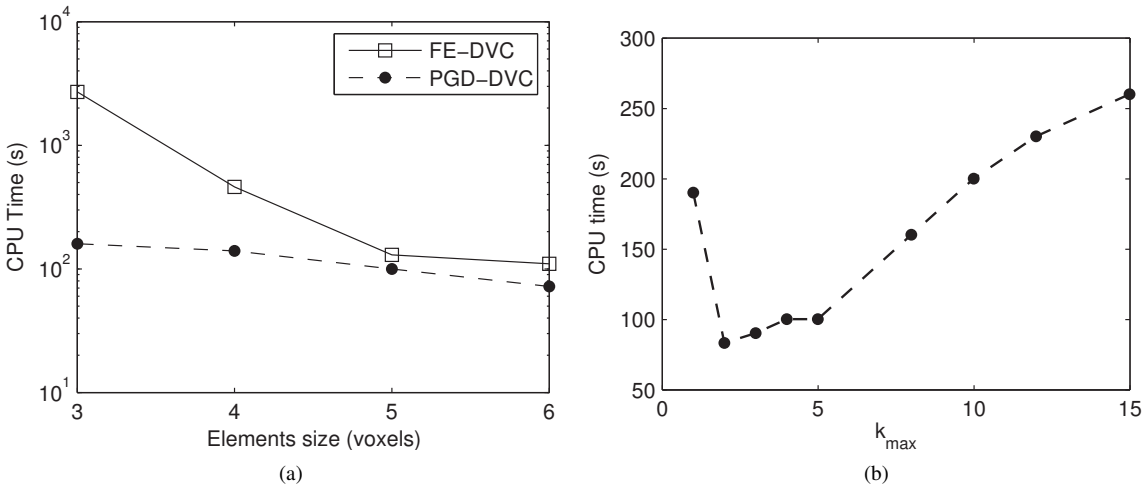

Figure 13: (a) CPU time as a function of the element size , for both methods, using the same regularization, initialization and ROI size. In this case, PGD-DVC considerably reduced the computational cost when using a fine discretization . (b) CPU time as a function of the maximum number of the fixed-point algorithm iterations, specified by the user. The same elements size, ROI and convergence criterion of the correlation problem (η_c) were used. Very few iterations of the fixed-point algorithm are needed for the convergence of the correlation problem.

mous reviewers for their valuable comments and suggestions to improve the quality of the paper.

References

1. A. Ammar, B. Mokdad, F. Chinesta, and R. Keunings. A new family of solvers for some classes of multidimensional partial differential equations encountered in kinetic theory modeling of complex fluids. Journal of Non-Newtonian Fluid Mechanics, 139:153–176, 2006.
2. M. Ben Azzouna, J.-N. Périé, J.-M. Guimard, F. Hild, and S. Roux. On the identification and validation of an anisotropic damage model using full-field measurements. International Journal of Damage Mechanics, 20(8):1130–1150, 2011.
3. B.K. Bay, T.S. Smith, D.P. Fyhrie, and M. Saad. Digital volume correlation: three-dimensional strain mapping using X-ray tomography. Experimental Mechanics, 39:217–226, 1999.
4. A. Benoit, S. Guérard, B. Gillet, G. Guillot, F. Hild, D. Mitton, J.-N. Périé, and S. Roux. 3D analysis from micro-MRI during in situ compression on cancellous bone. Journal of Biomechanics, 42(14):2381 – 2386, 2009.
5. G. Besnard, F. Hild, and S. Roux. Finite-element displacement fields analysis from digital images: Application to Portevin–Le Châtelier bands. Experimental Mechanics, 46:789–803, 2006.
6. B. Bognet, F. Bordeu, F. Chinesta, A. Leygue, and A. Poitou. Advanced simulation of models defined in plate geometries: 3D solutions with 2D computational complexity. Computer Methods in Applied Mechanics and Engineering, 201–204(0):1 – 12, 2012.
7. M. Chevreuil and A. Nouy. Model order reduction based on proper generalized decomposition for the propagation of uncertainties in structural dynamics. International Journal for Numerical Methods in Engineering, 89(2):241–268, 2012.
8. F. Chinesta, P. Ladeveze, and E. Cueto. A short review on model order reduction based on proper generalized decomposition. Archives of Computational Methods in Engineering, 18:395–404, 2011.
9. J. Fehrenbach and M. Masmoudi. A fast algorithm for image registration. Comptes Rendus Mathematique, 346(9–10):593 – 598, 2008.
10. E. Florentin and G. Lubineau. Identification of the parameters of an elastic material model using the constitutive equation gap method. Computational Mechanics, 46:521–531, 2010.
11. F. Forsberg, R. Mooser, M. Arnold, E. Hack, and P. Wyss. 3D micro-scale deformations of wood in bending: Synchrotron radiation μCT data analyzed with digital volume correlation. Journal of Structural Biology, 164:255–262, 2008.
12. L. Giraldi, A. Nouy, G. Legrain, and P. Cartraud. Tensor-based methods for numerical homogenization from high-resolution images. Computer Methods in Applied Mechanics and Engineering, 2012.
13. F. Hild, E. Maire, S. Roux, and J.-F. Witz. Three-dimensional analysis of a compression test on stone wool. Acta Materialia, 57(11):3310 – 3320, 2009.
14. F. Hild, B. Raka, M. Baudequin, S. Roux, and F. Cantelaube. Multi-scale displacement field measurements of compressed mineral wool samples by digital image correlation. Applied Optics, 32:6815–6828, 2002.
15. F. Hild and S. Roux. Comparison of local and global approaches to digital image correlation. Experimental Mechanics, pages 1–17, 2012.
16. B.K.P. Horn and B.G. Schunk. Determining optical flow. Artificial Intelligence, 18:185–203, 1981.
17. P. Ladevèze. New algorithms: mechanical framework and development (in french). Technical Report 57, LMT-Cachan, 1985.
18. P. Ladevèze, J.-C. Passieux, and D. Néron. The LATIN multiscale computational method and the proper generalized decomposition. Computer Methods in Applied Mechanics and Engineering, 199(21):1287–1296, 2010.
19. H. Leclerc, J.-N. Périé, S. Roux, and F. Hild. Integrated digital image correlation for the identification of mechanical properties. volume 5496 of Lecture Notes in Computer Science, pages 161–171. 2009.
20. H. Leclerc, J.-N. Périé, S. Roux, and F. Hild. Voxel-scale digital volume correlation. Experimental Mechanics, 51:479–490, 2011.
21. S.A. McDonald, F. Motazedian, A.C.F. Cocks, and P.J. Withers. Shear cracking in an Al powder compact studied by X-ray microtomography. Materials Science and Engineering: A, 508(1–2):64 – 70, 2009.
22. A. Mitiche and P. Bouthemy. Computation and analysis of image motion: A synopsis of current problems and methods. International Journal of Computer Vision, 19:29–55, 1996.
23. A. Nouy. A generalized spectral decomposition technique to solve a class of linear stochastic partial differential equations. Computer Methods in Applied Mechanics and Engineering, 196(45–48):4521 – 4537, 2007.
24. J.-J. Orteu, D. Garcia, L. Robert, and F. Bugarin. A speckle texture image generator. Proceedings of SPIE, the International Society for Optical Engineering, 6341:63410H–63410H–6, 2006.
25. J.-C. Passieux, P. Ladevèze, and D. Néron. A scalable time–space multiscale domain decomposition method: adaptive time scale separation. Computational Mechanics, 46:621–633, 2010.
26. J.-C. Passieux, J.-N. Périé, and L.A. Gomes Perini. A pgd approach to reduce the dimensionality of FE-based digital image correlation. In Optical Measurement Techniques for Systems & Structures^2, Shaker Verlag, ISBN:978-90-423-0419-2, pages 293–302, 2012.
27. J.-C. Passieux and J.-N. Périé. High resolution digital image correlation using proper generalized decomposition: PGD-DIC. International Journal for Numerical Methods in Engineering, 92:531–550, 2012.
28. K. Perlin. An image synthesizer. ACM SIGGRAPH Computer Graphics, 19(3), 1985.
29. E. Pruliere, F. Chinesta, and A. Ammar. On the deterministic solution of multidimensional parametric models using the proper generalized decomposition. Mathematics and Computers in Simulation, 81(4), 2010.
30. Johann Rannou, Nathalie Limodin, Julien Réthoré, Anthony Gravouil, Wolfgang Ludwig, Marie-Christine Baïetto-Dubourg, Jean-Yves Buffière, Alain Combescure, François Hild, and Stéphane Roux. Three dimensional experimental and numerical multiscale analysis of a fatigue crack. Computer Methods in Applied Mechanics and Engineering, 199(21–22):1307 – 1325, 2010.
31. S. Roux, F. Hild, P. Viot, and D. Bernard. Three-dimensional image correlation from X-ray computed tomography of solid foam. Composites Part A: Applied Science and Manufacturing, 39(8):1253 –

1265, 2008.
32. S. Roux, J. Réthoré, and F. Hild. Digital image correlation and fracture: an advanced technique for estimating stress intensity factors of 2D and 3D cracks. Journal of Physics D: Applied Physics, 42(21), 2009.
33. J. Réthoré, F. Hild, and S. Roux. Shear-band capturing using a multiscale extended digital image correlation technique. Computer Methods in Applied Mechanics and Engineering, 196(49–52):5016 – 5030, 2007.
34. M. Sjödahl, C.R. Siviour, and F. Forsberg. Digital volume correlation applied to compaction of granular materials. Procedia IUTAM, 4(0):179 – 195, 2012. IUTAM Symposium on Full-field Measurements and Identification in Solid Mechanics Cachan, France 4-8 July 2011.
35. Y. Sun, J.H.L. Pang, C.K. Wong, and F. Su. Finite element formulation for a digital image correlation method. Applied Optics, 44, 2005.
36. M.A. Sutton, W.J. Wolters, W.H. Peters, W.F. Ranson, and S.R. McNeill. Determination of displacements using an improved digital correlation method. Image and Vision Computing, 1(3):133–139, 1983.
37. B. Wagne, S. Roux, and F. Hild. Spectral approach to displacement evaluation from image analysis. The European Physical Journal Applied Physics, 17:247–252, 2002.

